JOURNAL OF MECHANICS OF CONTINUA AND MATHEMATICAL SCIENCES
www.journalimcms.org

ISSN (Online) : 2454 -7190 Vol.-21, No.-11, November (2026) pp 115-130 ISSN (Print) 0973-

ROLE OF PRINTING PARAMETERS ON THE MECHANICAL AND THERMAL PROPERTIES OF WOOD–WALNUT BIOCOMPOSITE, PLA AND ABS IN FDM

Raghavendra Prasad Nayak B[1], S. Krishnan[2], V. Diwakar Reddy[3]

[1,2] Department of Mechanical Engineering, Annamalai University, Chidambaram, Tamil Nadu, India.

[3]Department of Mechanical Engineering, S V University College of Engineering, Sri Venkateswara University - Tirupati, Andhra Pradesh, India

Email: [1]raghu536@gmail.com, [2]sk361977@gmail.com, [3]drsvuce@gmail.com

Corresponding Author: **Raghavendra Prasad Nayak B.**

https://doi.org/10.26782/jmcms.2026.11.00006

(Received: August 17, 2026; Revised: October 19, 2026; Accepted: November 08, 2026)

Abstract

In modern manufacturing, cost-effectiveness and environmentally friendly production processes play vital roles. Among them, Additive Manufacturing (AM) and 3D printing (3DP) technologies are key drivers of material savings in manufacturing engineering. Various plastic and composite materials are suitable for 3D printing by the deposition of semi-melted materials. Unfortunately, most materials suitable for fused deposition modeling (FDM) 3D printing are non-biodegradable, petroleum-based polymers. The current ecological crisis caused by plastic waste has generated significant interest in biodegradable materials for many applications, including 3D printing. As biodegradable thermoplastics increasingly penetrate the market, filaments for FDM 3D printing and fillers in the form of natural fibers are viable. They have the clear advantage of reducing costs while retaining the biodegradable characteristics of filaments. However, most biodegradable polymers, including Polylactic Acid (PLA), have insufficient mechanical properties for many applications. One approach to overcome this challenge is to introduce additives (bio-natural chemicals) that enhance the mechanical properties and maintain FDM 3D printability. The present study focuses on eco-friendly 3D printing, which reduces environmental impact, and the feasibility of implementing biodegradable components.

Keywords: 3D printing, Fused Deposition Modeling, ABS, PLA composite, waste wood - walnut shells

I. Introduction

Three-dimensional (3D) printing has opened a world of manufacturing possibilities. This additive manufacturing process produces both simple and highly complex parts quickly and at low cost. Various types of 3D printing technologies are currently used. However, many of them follow the same broadly defined working

principle: the 3D printer heats a material to a semi-molten state and deposits it layer by layer using information from a computer-aided design (CAD) model until the part is formed. The 3D printing process requires materials to undergo melting, reshaping, and resolidification or curing without significant changes in the mechanical properties of the 3D-printed samples [XV, XIX]. Consequently, thermoplastics, which possess the required characteristics, are the most commonly used materials in 3D printing. However, most of these plastics are not biodegradable. If not properly disposed of, they pose a risk to the environment. Therefore, significant efforts have been made to develop biodegradable (environmentally friendly) materials that are compatible with 3D printing and can be used to create fully functional parts [XIII, XVII]. Biodegradable 3D printing materials that are already available on the market, such as PLA and PLA Plus, and those still being developed for efficient 3D printing are discussed in these studies.

II. Composition and Fabrication of Filaments

This study aimed to investigate the feasibility and performance of biodegradable composite filaments made from waste wood and walnut shell particles combined with Polylactic acid (PLA), petroleum-based materials such as acrylonitrile butadiene styrene (ABS), and plant-based PLA. The integration of waste wood and walnut shell bio-fillers into Polylactic acid matrices provides a robust and sustainable strategy for additive manufacturing, effectively addressing the limitations of traditional petroleum-based polymers and presenting an innovative approach for utilizing agricultural and industrial waste, thereby contributing to a circular economy [V, XI]. These materials were chosen for their biodegradability, availability, and potential to improve the mechanical properties of the final printed product while minimizing waste [XVI]. The process comprises filament extrusion and 3D printing of specimens at 100% infill using the FDM method. Various material properties, such as tensile strength, flexibility, and degradation rates, were analyzed to assess the performance of the composite filaments. Additionally, the environmental impact of using these alternative materials was compared with that of traditional filaments, focusing on factors such as waste reduction and resource sustainability. This study aimed to provide valuable insights into the potential applications of biodegradable composite materials in FDM 3D printing, contributing to more sustainable manufacturing practices while reducing dependence on conventional, non-biodegradable materials.

Composition

- Waste wood filament is composed of 20% waste wood and 80% polylactic acid.
- Walnut shell filament is composed of 20% walnut shells and 80% polylactic acid.
- The polylactic acid (PLA) filament is 100% plant-based.
- Acrylonitrile Butadiene Styrene (ABS) filament is composed of 100% ABS.

Specimen

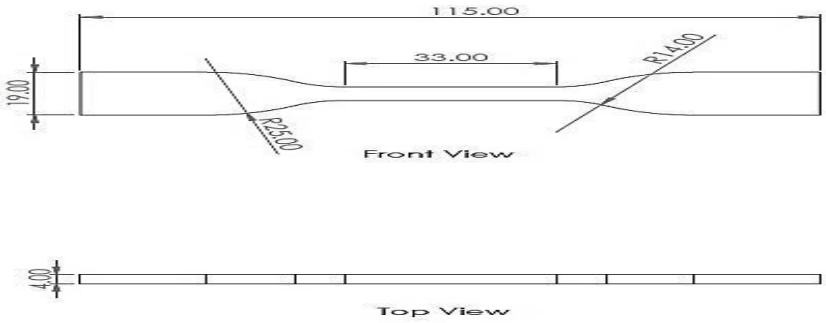


Fig. 1: Geometry of the ASTM D638 Type IV tensile test specimen

Fig. 1 illustrates that the tensile test specimens were designed in strict accordance with the ASTM D638 Type IV specification [XIV]. The tensile tests were conducted at a cross-head speed of 5 mm/min, because brittle materials require a controlled speed to ensure accurate results. The Type IV geometry is a standard for evaluating the tensile properties of rigid plastic materials, particularly when limited material quantities or non-standard fabrication setups are used. The nominal dimensions of the dog-bone specimens were as follows: total length, 115 mm; gauge length, 25 mm; width of the narrow section, 6 mm; and nominal thickness, 4 mm.

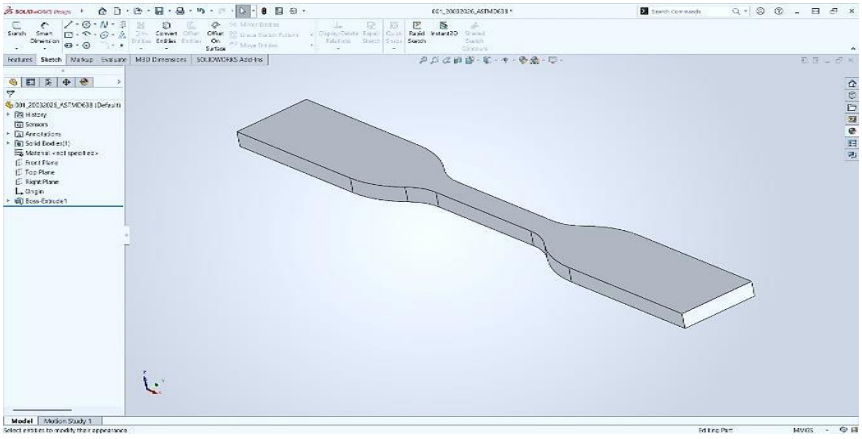


Fig. 2. Isometric view of the Type IV ASTM D638 specimen modeled in SolidWorks

Fig. 2 illustrates that the 2D image was converted to 3D using SolidWorks software, confirming the CAD modeling stage of this study and displaying the exact ASTM D638 Type IV dog-bone specimen described in the methodology. This 3D model serves as the foundational geometry before it is exported (typically as an STL or 3MF file) into slicing software to apply the three printing configurations (0°, 45°, and 90°).

Fabrication of specimens

The digital solid model of the ASTM D638 Type IV specimen was exported from the CAD environment as a high-resolution Standard Tessellation Language (.STL) file to minimize geometric discretization errors. The file was processed using open-source

slicing software (UltiMaker Cura v5.10.x) to generate distinct G-code files required for the manufacturing process. The fabrication was executed using a Siemens Bst fused deposition modeling machine equipped with a standard 0.4 mm brass nozzle. Process parameters, including 100% infill, standardized wall counts, and controlled deposition temperatures, were used to optimize filler-matrix adhesion and structural performance.

Table 1: Printing specimen parameters

Factor	Layer Thickness (A)	Orientation (B)	Speed (C)
Level 1	0.12 mm	0°	30 mm/s
Level 2	0.16 mm	45°	45 mm/s
Level 3	0.20 mm	90°	60 mm/s

To evaluate the coupled effects of spatial orientation and deposition dynamics on the mechanical profile of Type IV specimens, a structured three-tier experimental matrix for printing was used (Table 1).

The three printing parameters were selected for fabricating the FDM 3D-printed specimens. The experimental design considered layer thickness (A), build orientation (B), and printing speed (C) as the primary process variables. Layer thickness was varied at 0.12 mm, 0.16 mm, and 0.20 mm, while the build orientation was set to 0°, 45°, and 90° to investigate the effect of printing direction. Printing speed was evaluated at 30 mm/s, 45 mm/s, and 60 mm/s. These three factors, each at three levels, were selected to examine their influence on the print quality and mechanical performance of the fabricated specimens. For each material, the three factors were assigned to nine experimental runs using a Taguchi L9 (3^3) orthogonal array, and three independent specimens were fabricated and tested for each run. The complete run matrix, giving the layer thickness, raster orientation, printing speed, and measured tensile strength of every run, is presented in Table 7.

In the 0° print configuration, continuous longitudinal path profiles were generated from the CAD model directly along the primary axis of tension, reducing structural discontinuities in the narrow neck. In the model with a 90° vertical orientation, the curved transition zones between the wide-grip section and the narrow-gauge section exhibited a pronounced "stair-casing" effect. The 45° inclined specimen cohort represents a complex spatial compromise between the fully horizontal 0° and vertical 90° production regimes. In this configuration, the longitudinal axis of the ASTM D638 Type IV specimen is tilted at a 45° angle relative to the horizontal build plate (X-Y plane), necessitating the fabrication of a specialized sacrificial support-structure matrix to anchor the overhanging geometry during deposition.



(A) (B) (C) (D)

Fig. 3. Samples (A) waste wood (B) walnut (C) PLA (D) ABS

The standard ASTM D638 specimen was designed in SolidWorks and printed using the Siemens Bst fused deposition modeling (FDM) machine with a nozzle diameter of 0.4 mm and an infill density of 100% to produce filled specimens. The layer height was set to 0.12, 0.16, or 0.20 mm and the printing speed to 30, 45, or 60 mm/s, as specified for each run in Table 7. The nozzle temperature was maintained at 210 °C, and the build-platform temperature at 60 °C throughout the printing process; the same nozzle and bed temperatures were used for all four material groups. The specimens were fabricated from the four materials listed in Section II, and every printed specimen was inspected to confirm that there were no visible printing flaws. Three independent specimens were printed for each run so that the tension test could be repeated three times for every parameter combination.

Figure 3 shows the four distinct material groups that were investigated: a waste wood (20%) - PLA (80%) matrix composite filament (Figure 3A), walnut (20%) - reinforced PLA (80%) matrix composite filament (Figure 3B), unreinforced PLA filament (Figure 3C), and standard ABS plastic (Figure 3D). The geometric profile of the Type IV tensile specimens was constructed using computer-aided design (CAD) environments in strict accordance with the ASTM D638 dimensional specifications. The files were exported to the standard tessellation language (.STL) format and transferred to the slicing engine to establish toolpath trajectories.

After printing, the specimens were allowed to fully cool, gently detached from the platform, and subjected to metrological evaluation to verify their geometric tolerances and surface topography before destructive mechanical testing.

III. Results and Discussion

Testing was conducted using a Universal Testing Machine (UTM) (Model: ZY 2075-A). The tensile test was performed at a constant cross-head speed of 5 mm/min until specimen failure, as shown in Figure 4. For each material, the experiment followed the Taguchi L9 (3^3) orthogonal array described in Section II, in which layer thickness, raster orientation and printing speed were assigned to nine runs (Table 7); material type was treated as a separate grouping variable and not as a factor of the array. A full factorial design was therefore not used. In total, 36 unique material–parameter combinations (nine runs each for waste wood, walnut, PLA and ABS; Figure 4A–D) were tested. Three independent specimens were fabricated and tested for each combination (108 specimens in total), and the tensile strengths

reported in Tables 2–5 and Table 7 are the mean values of the three specimens of each run.



(A) (B) (C) (D)

Fig. 4: Samples after tensile testing (A) waste wood (B) walnut (C) PLA (D) ABS

PLA and ABS showed characteristic signs of polymer deformation. In some 0° unfilled specimens, slight stress-induced irregular tearing was visible, indicating localized plastic deformation and ductile tearing before ultimate failure. Wood-based biocomposites act as local stress concentrators in the polymer matrix, limiting polymer chain mobility, accelerating microcrack propagation, and shifting the failure mode from semi-ductile to highly brittle [VI].

Tensile strength of wastewood-reinforced composites

In Table 2, the wood composites showed the highest tensile strength at a 0° raster angle. The maximum value was 43.21 MPa at a 0.12 mm layer height, which is attributed to the alignment of the polymer paths with the applied load. However, this value differs from the 43.10 MPa recorded at 0.20 mm by only 0.11 MPa, and such a small difference cannot be distinguished from specimen-to-specimen variation based on mean values alone. At 90°, the same mean value of 29.79 MPa was recorded at all three layer heights. This suggests that layer thickness had little effect on inter-filament bonding in this orientation; however, identical mean values do not by themselves establish statistical equivalence, and this observation requires confirmation by statistical comparison of the specimen-level data. The 45° configuration produced intermediate strengths of 27.67–34.17 MPa. Its mixed tensile and shear stresses produced distinct crack patterns.

Thermal degradation testing showed that heating the wood-filled biocomposites to 150°C for 10 minutes caused visible deformation, with structural failure initiating at approximately 148°C. Because this failure temperature falls below the prescribed 150°C exposure limit, the material cannot be considered thermally stable under these conditions, despite exhibiting adequate mechanical strength at room temperature. The results therefore indicate a clear trade-off between ambient-temperature tensile performance and thermal resistance. The brittle failure observed in the wood-filled specimens is attributed to the interruption of polymer chain continuity by the wood particles, which increase structural porosity, reduce interfacial bonding, and restrict efficient load transfer across adjacent layers.

These defects promote local stress concentration and accelerate crack initiation and propagation, thereby reducing the composite's ability to deform plastically before fracture [II].

Table 2: Tensile Strength characterisation of wastewood composite

S.No	Properties	Unit	Test Method	Result
1	Heat resistance	%	150°C/10 min	Deformation observed at 148°C
2	Layer height (mm) / Raster Angle (^{0})			Tensile Strength (MPa)
1)	0.12/0°		ASTM D 638	43.21
2)	0.12/45°		ASTM D 638	27.67
3)	0.12/90°		ASTM D 638	29.79
4)	0.16/0°		ASTM D 638	42.35
5)	0.16/45°		ASTM D 638	34.17
6)	0.16/90°		ASTM D 638	29.79
7)	0.2/0°		ASTM D 638	43.10
8)	0.2/45°		ASTM D 638	33.70
9)	0.2/90°		ASTM D 638	29.79

Tensile strength of Walnut-Reinforced composites

In Table 3, the 90° raster orientation substantially reduced tensile strength. The lowest value, 11.56 MPa, occurred at a 0.16 mm layer height. In this configuration, stress acts across the filament tracks, so that the bond lines offer less resistance. Consequently, failure shifts from filament breakage to interfacial debonding and delamination between deposited layers.

Table 3: Tensile Strength characterisation of walnut shells composite

S.No	Properties	Unit	Test Method	Result
1	Heat resistance	%	150°C/10 min	Deformation observed at 133°C
2	Layer height (mm) / Raster Angle (^{0})			Tensile Strength (MPa)
1)	0.12/0°		ASTM D 638	37.22
2)	0.12/45°		ASTM D 638	15.47
3)	0.12/90°		ASTM D 638	14.76
4)	0.16/0°		ASTM D 638	37.06
5)	0.16/45°		ASTM D 638	18.26
6)	0.16/90°		ASTM D 638	11.56
7)	0.2/0°		ASTM D 638	38.79
8)	0.2/45°		ASTM D 638	28.68
9)	0.2/90°		ASTM D 638	15.14

The walnut composites printed at a 0° raster angle showed the highest tensile strength. The maximum value was 38.79 MPa at a 0.20 mm layer height. In this orientation, the tensile load acts parallel to the extruded strands, allowing them to share the applied force. Failure therefore occurs mainly through strand rupture rather than inter-bead separation.

Thermal degradation experiments, in which walnut-composite specimens were exposed to 150°C for 10 minutes, showed that structural failure occurred at 133°C,

17°C below the prescribed exposure temperature. This result shows that the material does not meet the 150°C thermal-resistance limit under the tested conditions. The reduced thermal tolerance is primarily due to the walnut particles, which interrupt biopolymer chain continuity and weaken interfacial bonding within the matrix. In addition, residual moisture and voids associated with the natural filler can promote localized heat accumulation, differential thermal expansion, and premature matrix relaxation. These effects intensify warping and damage along weak interlayer bonds before the polymer reaches its typical melting point, confirming that the walnut composite's mechanical performance at room temperature is accompanied by poor resistance to elevated temperatures.

Tensile strength of PLA

In Table 4, PLA specimens reached a maximum tensile strength of 47.39 MPa at a 0.20 mm layer height and a 0° raster angle. The aligned strands carry the load efficiently along the print direction. At 90°, tensile strength falls to 5.98 MPa at a 0.16 mm layer height, an approximate 87% reduction. Here, the stress acts perpendicular to the print tracks, making the interlayer bond lines the primary failure sites.

Table 4: Tensile Strength characterisation of PLA

S.No	Properties	Unit	Test Method	Result
1	Heat resistance	%	150°C/10 min	Deformation observed at 145°C
2	Layer height (mm) / Raster Angle (^{0})			Tensile Strength (MPa)
1)	0.12/0°		ASTM D 638	41.23
2)	0.12/45°		ASTM D 638	23.64
3)	0.12/90°		ASTM D 638	18.74
4)	0.16/0°		ASTM D 638	39.80
5)	0.16/45°		ASTM D 638	23.85
6)	0.16/90°		ASTM D 638	5.98
7)	0.2/0°		ASTM D 638	47.39
8)	0.2/45°		ASTM D 638	21.71
9)	0.2/90°		ASTM D 638	8.55

Thermal degradation tests showed that all nine PLA specimens exposed to 150°C for 10 minutes underwent complete macroscopic deformation. The unreinforced PLA began to fail at approximately 145°C, while wood particles slightly improved thermal stability to 148°C; walnut-shell particles reduced it to 133°C, likely because of localized heat accumulation and volatile release. These results demonstrate that organic fillers alter PLA's thermal response, but none of the tested materials remained stable at 150°C as the polymer transitioned from a rigid non-crystalline state to a soft melt phase.

Tensile strength of ABS

In Table 5, ABS specimens reached a maximum tensile strength of 44.68 MPa at a 0.16 mm layer height and a 0° raster angle. At this orientation, the tensile load acts parallel to the continuous polymer strands. Both the rubber-like butadiene phase and the rigid acrylonitrile–styrene phase contribute to load bearing. This alignment delays

crack initiation and promotes strand yielding. When the raster angle increased to 90°, tensile strength decreased sharply to 9.96 MPa.

Table 5: Tensile Strength characterisation of ABS

S.No	Properties	Unit	Test Method	Result
1	Heat resistance	%	150°C/10 min	Deformation observed at 212°C
2	Layer height (mm) / Raster Angle (^{0})			Tensile Strength (MPa)
1)	0.12/0°		ASTM D 638	39.75
2)	0.12/45°		ASTM D 638	26.71
3)	0.12/90°		ASTM D 638	23.44
4)	0.16/0°		ASTM D 638	44.68
5)	0.16/45°		ASTM D 638	30.41
6)	0.16/90°		ASTM D 638	9.96
7)	0.2/0°		ASTM D 638	42.45
8)	0.2/45°		ASTM D 638	25.43
9)	0.2/90°		ASTM D 638	12.99

This notable reduction, approximately a 77% decrease from the peak, indicates that under transverse loading, the mechanical performance is mainly associated with the integrity of the inter-filament interfaces. Owing to the high coefficient of thermal contraction of ABS [I], considerable residual stresses develop during cooling, potentially diminishing polymer chain entanglement between adjacent rasters and resulting in premature delamination. To assess thermal degradation and establish environmental thresholds, unmodified ABS specimens were exposed for 10 minutes at 150°C.

Macrostructural deformation was observed in all the samples. Although ABS has a higher glass transition temperature (Tg ≈ 105°C) [XX] than PLA and thus offers greater resilience to moderately elevated temperatures, exposure to 150°C exceeds this limit by nearly 45°C. ABS has a practical thermal operating range limited by its glass transition temperature, with significant reduction in structural performance occurring above 100-120°C, while still maintaining strong mechanical performance (44.68 MPa at 0.16 mm at 0°). This remarkable heat resistance is due to the entanglement of the amorphous terpolymer chain in ABS, which provides superior stability under extreme temperatures compared to bio-composites.

Hardness Test

Shore D hardness testing (ASTM D2240) assesses material resistance to surface indentation by applying a controlled load [XVIII]. This measurement is used to characterize the mechanical performance and surface properties of FDM-printed specimens.

Table 6: Hardness test for composite materials

S.No	Materials	Properties	Unit	Test Method	Result
1	Waste wood	Hardness	Shore D	ASTM D 2240	75,77,76,75,76
2	Walnut shells	Hardness	Shore D	ASTM D 2240	72,71,73,70,71
3	PLA	Hardness	Shore D	ASTM D 2240	77,78,77,76,77
4	ABS	Hardness	Shore D	ASTM D 2240	72,70,71,70,71

As shown in Table 6, PLA showed the highest overall hardness baseline at 77.00 ± 0.71 Shore D, attributable to its semi-crystalline structure and dense molecular arrangement. The rigid crystalline domains efficiently inhibited penetration by the durometer indenter tip.

ABS exhibited a considerably lower hardness value of 70.80 ± 0.84 Shore D, reflecting an approximate 8% reduction compared with PLA. As an amorphous terpolymer with an elastomeric polybutadiene phase, ABS exhibits inherently lower surface modulus and greater molecular compliance, facilitating deeper elastic indentation under a constant load [I].

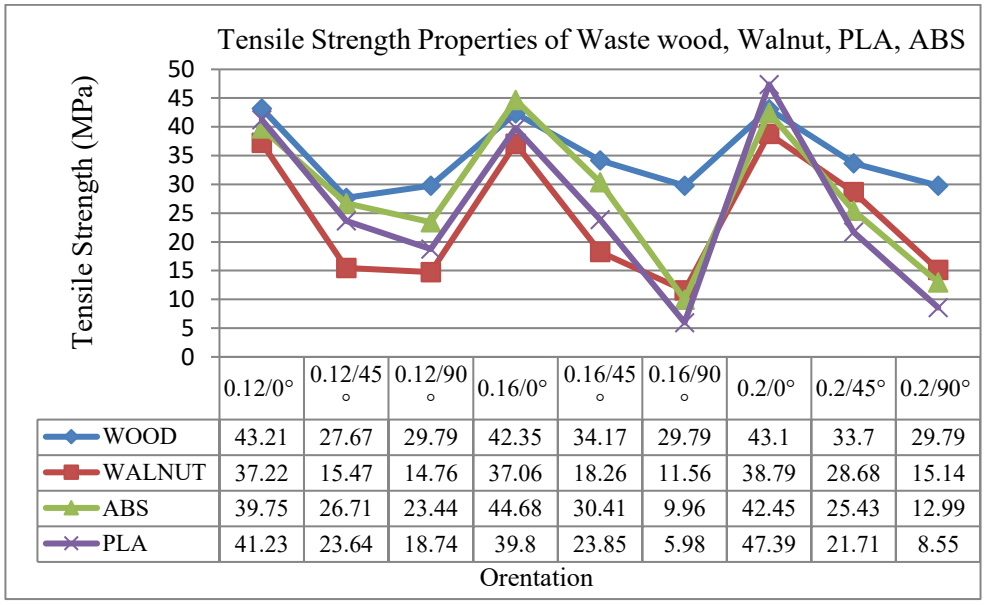
The waste wood composite maintained a robust surface hardness of 75.80 ± 0.84 Shore D, amounting to only a 1.5% decrease relative to PLA. The high aspect ratio of wood sawdust fibers enables tight interlocking within the polymer melt, allowing these fibers to function as localized stress-bearing networks that effectively distribute the indentation force throughout the matrix.

Conversely, the walnut composite exhibited a significant reduction in hardness to 71.40 ± 1.14 Shore D, a clear decline from that of PLA. Walnut shell particles, which are spherical, dense, and rigid, have a smooth and low-aspect-ratio geometry that limits their ability to physically interlock with polymer chains. This results in suboptimal interfacial wetting and microscopic air gaps.

Overall, PLA's superior surface hardness (77.00 Shore D) is attributed to its semi-crystalline backbone, while the integration of fibrous waste wood particles sustains this property (75.80 Shore D) through effective mechanical interlocking.

Tensile strength of different composites

In Figure 5, when examining the layer thickness, printing at a 0° raster angle consistently resulted in a marked improvement in mechanical properties. This is evidenced by three notable peaks observed in the data at (0.12/0°), (0.16/0°), and (0.20/0°). The highest tensile strength was achieved with PLA at 0.20/0°, recording 47.39 MPa, followed closely by ABS at 0.16/0° (44.68 MPa).



	0.12/0°	0.12/45°	0.12/90°	0.16/0°	0.16/45°	0.16/90°	0.2/0°	0.2/45°	0.2/90°
WOOD	43.21	27.67	29.79	42.35	34.17	29.79	43.1	33.7	29.79
WALNUT	37.22	15.47	14.76	37.06	18.26	11.56	38.79	28.68	15.14
ABS	39.75	26.71	23.44	44.68	30.41	9.96	42.45	25.43	12.99
PLA	41.23	23.64	18.74	39.8	23.85	5.98	47.39	21.71	8.55

Fig. 5. Tensile Strength Properties of PLA, ABS, Walnut, Waste Wood

Fused deposition modeling (FDM) components are susceptible to inter-bead-weld-line delamination under perpendicular loading conditions [IV]. The most pronounced reduction in mechanical performance occurred in PLA at 0.16/90°, where the tensile strength decreased to 5.98 MPa, representing an approximate 87% reduction compared to its maximum value in the longitudinal direction.

The wood composite exhibits a consistent horizontal trend at a 90° raster angle. While the strengths of PLA, ABS, and walnut vary between 5.98 MPa and 23.44 MPa depending on layer thickness, the wood composite recorded the same mean value of 29.79 MPa at all tested heights (0.12 mm, 0.16 mm, and 0.20 mm). At the critical 90° orientation, characterized as the weakest direction, wood composites recorded the highest mean tensile strength among the tested materials. For example, at a layer thickness of 0.16 mm, wood (29.79 MPa) outperformed ABS (9.96 MPa) and PLA (5.98 MPa).

These findings suggest that the high aspect ratio of the fibrous waste wood particles may bridge the inter-bead weld boundaries, with the fibers functioning as structural microanchors that enhance the stability of the transverse matrix. Consequently, the adverse effects typically associated with an increased layer height appeared smaller for the wood composite. Because this comparison is based on mean values without a formal statistical test, the reduced anisotropy should be regarded as indicative and requires confirmation by specimen-level statistical analysis.

Taguchi analysis

The Taguchi analysis was based on the L9 (3^3) orthogonal array given in Table 7, in which layer thickness (A), raster orientation (B), and printing speed (C) were each assigned the three levels listed in Table 1. Each run was printed and tested with three specimens, and the tensile strength data of each material were analysed separately in

MINITAB. Because a higher tensile strength is desired, the larger-is-better signal-to-noise (S/N) ratio was used, $S/N = -10 \log_{10}[(1/n)\ \Sigma(1/y_i^2)]$, where y_i is the measured tensile strength, and n is the number of observations per run. The optimal level of each factor was taken as the level with the highest mean S/N ratio in the main-effect plots (Fig. 6) [III].

Table 7: L9 orthogonal array run matrix and mean tensile strength of each material (three specimens per run)

Run	Layer thickness A (mm)	Raster orientation B (°)	Printing speed C (mm/s)	Waste wood UTS (MPa)	Walnut UTS (MPa)	PLA UTS (MPa)	ABS UTS (MPa)
1	0.12	0	30	43.21	37.22	41.23	39.75
2	0.12	45	45	27.67	15.47	23.64	26.71
3	0.12	90	60	29.79	14.76	18.74	23.44
4	0.16	0	45	42.35	37.06	39.80	44.68
5	0.16	45	60	34.17	18.26	23.85	30.41
6	0.16	90	30	29.79	11.56	5.98	9.96
7	0.20	0	60	43.10	38.79	47.39	42.45
8	0.20	45	30	33.70	28.68	21.71	25.43
9	0.20	90	45	29.79	15.14	8.55	12.99

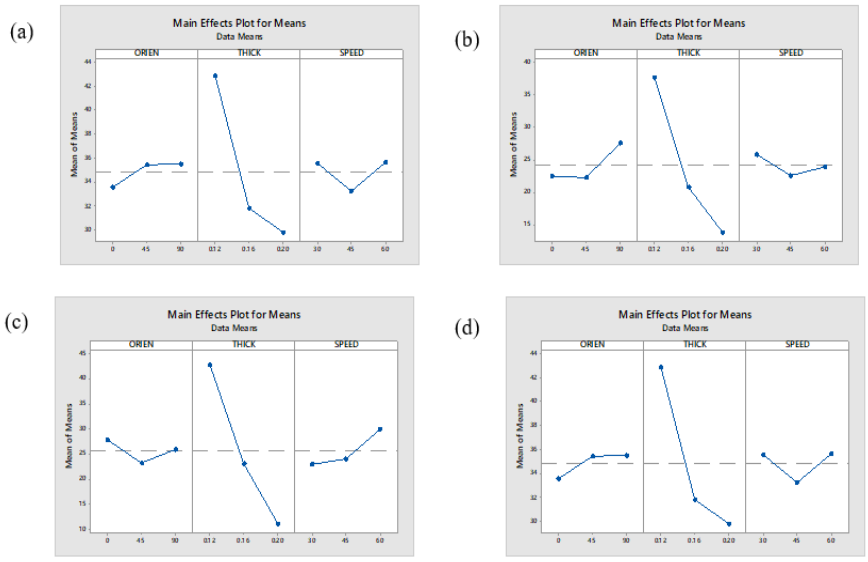


Fig. 6. Main effect plot for SN ratios of composite materials (a) Waste wood, (b) Walnut, (c) PLA, (d) ABS

In Figure 6a, the main effects plot identifies layer thickness as the most influential parameter affecting the tensile strength of the waste wood (Figure 6a), followed by printing speed and orientation. The optimal conditions for achieving higher tensile strength appear to be a lower layer thickness (0.12 mm/0°), appropriate printing orientation, and moderate printing speed. These findings highlight the importance of optimizing printing parameters to improve the mechanical performance of 3D-printed

biodegradable composite materials: 90° orientation, 0.12 mm layer thickness, and 30 mm/sec print speed.

Figure 6b shows the main effects plot for S/N ratios and means, which indicates the optimum levels for the tensile strength of the walnut material. The obtained plots were created using the "Larger is better" principle; the larger the value, the stronger the material.

Figure 6c (PLA): the main effects plot for S/N and means indicates the optimum levels of tensile strength for the PLA material. The resultant plots were constructed using the principle of Larger is better because we needed to evaluate the material's tensile strength, which should be high. The acquired levels for this PLA material were 0° orientation, 0.2 mm layer thickness, and 60 mm/s print speed.

Figure 6d (ABS): the main effects plot for S/N and means indicates the optimum levels of tensile strength for the ABS material. The resultant plots were constructed using the principle of Larger is better because we needed to evaluate the material's tensile strength, which should be high. The acquired levels for ABS were 0° orientation, 0.16 mm layer thickness, and 30 mm/s print speed [VII].

IV. Conclusions

This study examined the influences of material composition (PLA, ABS, wood composite, and walnut-shell composite), layer thickness (0.12, 0.16, and 0.20 mm), raster orientation (0°, 45°, and 90°), and printing speed (30, 45, and 60 mm/s; assigned through an L9 orthogonal array with three specimens per run) on the mechanical, surface, and thermal characteristics of FDM-fabricated components**.**

Mechanical anisotropy: The ultimate tensile strength (UTS) is primarily governed by the printing raster orientation. Across all materials, a 0° longitudinal orientation maximized the load-bearing efficiency by aligning the polymer chains parallel to the direction of the applied force, achieving a peak UTS of 47.39 MPa for PLA at a layer height of 0.20 mm. In contrast, a 90° transverse orientation positions the loading stress perpendicular to the print paths, altering the failure modes to inter-bead weld line delamination.

Structural stability of wood composites: While polymers such as PLA and ABS suffer significant tensile degradation at a 90° orientation (up to an 87% reduction, reaching a critical low of 5.98 MPa for PLA), the waste wood-plastic composite recorded the same mean transverse strength of 29.79 MPa at all layer heights, indicating a comparatively stable transverse response that requires confirmation by statistical analysis of the specimen-level data. This suggests that high-aspect-ratio wood fibers bridge adjacent printed tracks, improving local reinforcement and reducing defects caused by thicker layers.

Surface hardness: Indentation testing according to ASTM D2240 indicated that the surface resistance depends on the crystalline matrix behavior and filler morphology [VIII, XII]. PLA exhibited the highest rigidity (77.00 Shore D) owing to its semi-crystalline nature. The incorporation of wood particles preserved this resistance (75.80 Shore D) by enhancing mechanical interlocking [IX]. In contrast, the dense spherical geometry of walnut shell particles limited chain entanglement and

introduced localized microvoids, reducing the hardness to 71.40 Shore D, mirroring the ductile flexibility typical of amorphous ABS (70.80 Shore D).

For complex components subjected to multi-axial loading, where isotropic reliability is essential, waste wood composites appear promising owing to their comparatively high transverse tensile strength [X], subject to the limitations noted below.

Limitations: The tensile strengths are reported as mean values of three specimens per run; standard deviations, confidence intervals and formal statistical comparisons of the material and process-factor effects are not reported, and the Taguchi main-effect trends should therefore be regarded as indicative. Complete stress–strain curves, elastic modulus, elongation at break and failure-location records are not reported in this study. The filler particle-size distribution, drying conditions, moisture content, dispersion quality, filament extrusion temperature profile and filament diameter tolerance of the composite filaments, and the wall count, top/bottom layers, infill pattern, chamber and cooling settings, are likewise not reported. These aspects will be addressed in future work.

V. Acknowledgements

The authors would like to thank the management of Annamalai University and S V University College of Engineering for the facilities and support they provided.

Conflict of Interest:

The authors declare no conflict of interest.

References

I. Bano, S., et al. “Study of Surface Mechanical Characteristics of ABS/PC Blends Using Nanoindentation.” *Processes*, vol. 9, no. 4, 2021, p. 637, 10.3390/pr9040637.

II. Battini, D., et al. “Effects of Fiber Layout on Strength and Failure of 3D Printed Notched Composites.” *Composite Structures*, vol. 327, 2024, p. 117644. 10.1016/j.compstruct.2023.117644.

III. Boostan, A., et al. “Effect of Layer Thickness and Print Orientation on Surface Hardness of FDM-Printed PLA, PETG, PC.” *Proceedings of International Structural Engineering and Construction*, vol. 12, no. 1, 2025. 10.14455/isec.2025.12(1).mat-12.

IV. Draghici, S., et al. “Design and Fabrication of Thermoplastic Moulds for Manufacturing CFRP Composite Impeller Blades.” *Materiale Plastice*, vol. 57, no. 1, 2020, pp. 290–98. 10.37358/mp.20.1.5338.

V. Imran, K., et al. “Eco-Friendly 3D Printing—Biodegradable PLA Composites Reinforced with Wood Waste.” 2025, pp. 250–54. 10.1201/9781003725053-43.

VI. Jose, A. S., et al. "Investigations on Mechanical Properties of Bio-Waste Micro Particles Reinforced Phenol Formaldehyde Composites." *Archives of Metallurgy and Materials*, 2022, pp. 377–84. 10.24425/amm.2022.137768.

VII. Koren, K., et al. "Investigating the Strength Recovery of Additively Manufactured Components Repaired Utilizing a 3D Printing Pen." *Research Square*, 3 Aug. 2022. 10.21203/rs.3.rs-1902848/v1.

VIII. Kumar, P. Satish, et al. "A Study of Hardness and Microstructure of a Robot Deposited WAAM Component with Varying Wire Feed Rate in the Build Direction." *Journal of Mechanics of Continua and Mathematical Sciences*, vol. 15, no. 7, 2020, pp. 517–28. 10.26782/jmcms.2020.07.00045.

IX. Maguluri, Nagarjuna, et al. "A Review on the Development of Customized Ankle Foot Orthosis for Foot Drop Using Additive Manufacturing Processes." *Journal of Mechanics of Continua and Mathematical Sciences*, vol. 15, no. 7, 2020, pp. 661–74. 10.26782/jmcms.2020.07.00058.

X. Maheshbabu, Pidaparthy, et al. "Numerical Investigation of MWCNT/ZnO Hybrid Nanofluid Heat Performance of a Counter Flow Heat Exchanger." *Journal of Mechanics of Continua and Mathematical Sciences*, vol. 20, no. 7, 2025, pp. 136–53, 10.26782/jmcms.2025.07.00008.

XI. Meenakshi, C. M., et al. "Advanced Engineering Methods for Design, Fabrication and Analysis of Hybrid Fiber Reinforced Small HAWT Blade." *Journal of Mechanics of Continua and Mathematical Sciences*, Special Issue no. 2, 2019, pp. 707–19, 10.26782/jmcms.spl.2019.08.00086.

XII. Mogan, J., et al. "Fused Deposition Modelling of Polymer Composite: A Progress." *Polymers*, vol. 15, no. 1, 2023, p. 28. 10.3390/polym15010028.

XIII. Mohammed, Raffi, et al. "Future Trends and Emerging Technologies in Mechanical Engineering: An Analytical Perspective." *Journal of Mechanics of Continua and Mathematical Sciences*, vol. 20, no. 7, 2025, pp. 62–74. 10.26782/jmcms.2025.07.00004.

XIV. Raj, S. S., et al. "Philosophy of Selecting ASTM Standards for Mechanical Characterization of Polymers and Polymer Composites." *Materiale Plastice*, vol. 58, no. 3, 2021, pp. 247–56. 10.37358/mp.21.3.5523.

XV. Sola, A. "Materials Requirements in Fused Filament Fabrication: A Framework for the Design of Next-Generation 3D Printable Thermoplastics and Composites." *Macromolecular Materials and Engineering*, vol. 307, no. 10, 2022, p. 2200197. 10.1002/mame.202200197.

XVI. Song, X., et al. "Properties of Poly(lactic acid)/Walnut Shell/Hydroxyapatite Composites Prepared with Fused Deposition Modeling." *Scientific Reports*, vol. 12, no. 1, 2022, p. 11563. 10.1038/s41598-022-15622-8.

XVII. Subramani, R., et al. "Exploring the Use of Biodegradable Polymer Materials in Sustainable 3D Printing." *Applied Chemical Engineering*, vol. 7, no. 2, 2024, p. 3870. 10.59429/ace.v7i2.3870.

XVIII. Sultana, J., et al. "Influences of 3D Printing Parameters on the Mechanical Properties of Wood PLA Filament: An Experimental Analysis by Taguchi Method." *Progress in Additive Manufacturing*, vol. 9, no. 4, 2023, pp. 1239–51. 10.1007/s40964-023-00516-6.

XIX. Suresh, Gamini, et al. "Characterization of Materials for Customized AFO Using Additive Manufacturing." *Journal of Mechanics of Continua and Mathematical Sciences*, vol. 15, no. 7, 2020, pp. 587–96. 10.26782/jmcms.2020.07.00052.

XX. Wei, X., et al. "3D Printable Graphene Composite." *Scientific Reports*, vol. 5, 2015, p. 11181. 10.1038/srep11181.